

Durability of composite materials for nuclear energy systems

8

Kyle S. Brinkman¹, Rob Grote¹, Kenneth L. Reifsnider², Ye Cao², Russel Raihan², Vamsee Vadlamudi³

¹Clemson University, Clemson, SC, United States; ²Mechanical and Aerospace Engineering, University of Texas Arlington (UTA), Arlington, TX, United States; ³University of Texas Arlington Research Institute (UTARI), Fort Worth, TX, United States

Chapter outline

- 8.1 Introduction 314**
- 8.2 Mechanical properties of ceramics as pertains to the elemental release 315**
- 8.3 Corrosion/leaching studies of candidate single-phase and multiphase materials 317**
 - 8.3.1 Corrosion and leaching techniques 317
 - 8.3.2 PCT product characterization test 317
 - 8.3.3 MCC-1 monolith test 319
 - 8.3.4 Vapor hydration test 319
 - 8.3.5 Corrosion studies of glass waste forms 319
 - 8.3.6 Corrosion studies of multiphase waste forms 320
 - 8.3.6.1 SYNROC type waste forms C 320
 - 8.3.7 Corrosion studies of single-phase waste forms 321
 - 8.3.7.1 Zirconolite and pyrochlore 321
 - 8.3.7.2 Perovskite 321
 - 8.3.7.3 Hollandite 322
 - 8.3.8 Uranium dioxide 323
- 8.4 Radiation effects on surface, mechanical properties, and leaching 324**
 - 8.4.1 Radiation damage processes 324
 - 8.4.2 Radiation damage process for crystalline structures 324
 - 8.4.2.1 Frenkel pair defects 324
 - 8.4.2.2 Electronic defects 326
 - 8.4.2.3 Volume change 326
 - 8.4.2.4 Crystalline long-range order amorphization 326
 - 8.4.3 Radiation induced surface damage 329
 - 8.4.3.1 Amorphization 329
 - 8.4.3.2 The effect of volume expansion on the surface 329
 - 8.4.3.3 How radiation effects mechanical properties 330
 - 8.4.3.4 How radiation effects leaching 330
- 8.5 Morphology drivers for irreversible species diffusion and transport in HeteroFoams 331**
 - 8.5.1 Flux of an included species 331
- References 335**

8.1 Introduction

Legacy waste from national defense activities is currently being immobilized in glass vitrification facilities at the Savannah River Site in South Carolina and the Hanford Site in Washington State. Currently, commercial spent fuel is stored on-site in wet storage or dry cask storage facilities. The technology exists to reprocess the 96% of the remaining Uranium in spent nuclear fuel for further use; however, the resulting waste streams must be considered [1]. The ultimate composition of the streams depends on the separation process used but commonly have components of cesium and strontium streams, lanthanide streams, minor actinides, and transition metals.

Options to store this waste include encapsulation in glass or vitrification, crystalline ceramics, or some combination of the two approaches [2]. The resulting composite consisting of waste and host matrix is termed a waste form. Ceramics are a materials class defined by primarily ionic and covalent bonding with structural variations ranging from fully ordered crystalline (called as crystalline ceramics) to disordered amorphous (called as glass). Tailoring of a ceramic waste form is based on the knowledge that there are many naturally produced minerals containing radioactive and nonradioactive species very similar to the radionuclides of concern in wastes from fuel reprocessing. For instance, there are natural analogs of hollandite including anka-gite, found in dolomitic marble in the Apuan Alps in Tuscany, Italy. A hollandite-type crystal structure appears to be a good candidate for Cs immobilization [3]. A crystal structure called zirconolite is attractive for the immobilization of minor actinides. This is a relatively rare mineral in nature but found to exist in geological environments associated with silica-poor rocks [4]. Finally, perovskite and pyrochlore structures are attractive for the incorporation of lanthanide series elements and have known natural analogs [5].

Ultimately the waste form will be placed inside a metal canister, which will undergo storage in a geologic repository. The waste form can be considered a source term for the transport of radionuclides into the environment—the goal of international waste form efforts is to design materials with low release rates over geologic time scales.

The design of crystalline systems aims to take advantage of the long-term thermodynamic stability of crystalline ceramics to create more durable waste forms (as compared to high-level waste glass) to reduce the reliance on engineered and natural barrier systems. Titanate ceramics have been thoroughly studied for use in immobilizing nuclear wastes (e.g., the synthetic rock, or “SYNROC” family) due to their natural resistance to leaching in water. Assemblages of several titanate phases consisting of the following:

- a. Zirconolite—example, $\text{CaZrTi}_2\text{O}_7$
- b. Perovskite/Pyrochlore—example, $\text{NdTiO}_3/\text{Nd}_2\text{Ti}_2\text{O}_7$
- c. Hollandite—example, $\text{Ba}_1\text{Cs}_{0.28}\text{Al}_{1.46}\text{Fe}_{0.82}\text{Ti}_{5.72}\text{O}_{16}$

have been successfully demonstrated to incorporate radioactive waste elements, and the multiphase nature of these materials allows them to accommodate variation in the waste composition.

The focus of this chapter will be to review (1) mechanical properties, (2) corrosion and leaching effects, (3) radiation damage effects, and (4) morphology drivers for irreversible species diffusion and transport in model crystalline ceramic systems for the immobilization of waste streams resulting from potential commercial fuel reprocessing.

8.2 Mechanical properties of ceramics as pertains to the elemental release

In general, ceramic materials such as the ones used in SYNROC are brittle. Therefore, the mechanical properties are commonly measured by Vickers hardness and fracture toughness using indentation methods. The composition of each of the ceramic waste forms can have a significant effect on the toughness of the material.

Vickers hardness measurement is a technique used to measure the hardness of a material and compare it to other materials by using a Vickers hardness number. The Vickers hardness number for the material is calculated using Eq. (8.1),

$$HV = \frac{2 \times F \times \sin(136/2)}{\left(\frac{d1 + d2}{2}\right)^2} \quad (8.1)$$

The technique is pictured in Fig. 8.1, where force is applied with a diamond crystal; then, the dimensions of the indent are measured.

Indentation fracture toughness is estimated by a similar technique by measuring the crack length that results from indentation. The fracture toughness is then calculated by Eq. (8.2) [6]:

$$K_{IC} = k \left(\frac{E}{H}\right)^{1/2} \frac{F_m}{c^{3/2}} \quad (8.2)$$

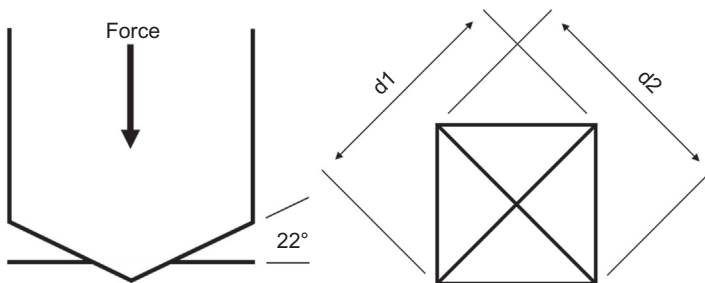


Figure 8.1 Vickers hardness testing diagram showing the indentation geometry of the diamond indentation tool and on the right, the measurements used for calculating the hardness from the resulting indentation mark.

where c is the crack length, F_m is load, E is Young's modulus, H is hardness, and k is a constant selected for the instrument tip, such as a Vickers type tip. Multiple different equations have been applied for calculating fracture toughness. Different equations lead to some minor deviation. For example, the K_{IC} of $\text{Li}_{0.33}\text{La}_{0.57}\text{TiO}_3$ can vary from 0.85 to about 1.2 $\text{MPa m}^{1/2}$ [6–8]. The fracture toughness range averages out to about 1 $\text{MPa m}^{1/2}$, which is similar to other ideal brittle materials, such as glasses [7]. A table of some of the mechanical properties of perovskite and pyrochlore is given in Table 8.1.

As specifically shown for perovskites, though true for the other SYNROC phases, the processing temperature, processing technique, microstructure as well as the A and B site cation species have an impact on the mechanical properties [6–9]. At room temperature, the Li doping fraction has a minor effect on Young's modulus as it only varied between 154 and 182 GPa as x was increased from 0.30 to 0.37 [6]. Similarly, in two other studies of $\text{Li}_{0.33}\text{La}_{0.57}\text{TiO}_3$ Young's modulus varied between 186 and 200 GPa depending on the microstructure properties [7,8]. However, at elevated temperatures, between 1000 and 1300°C, the elastic moduli of a $\text{Li}_x\text{LaAlO}_3$ decreased from 63.07 to 24.7 with increasing temperature while the fracture toughness was significantly high at about 3.15 $\text{MPa m}^{1/2}$ [9]. The Vicker's hardness of $\text{Li}_{0.33}\text{La}_{0.57}\text{TiO}_3$ ranged from 8.4 to 9.7 GPa and was primarily effected by the porosity [7,8].

In comparison, pyrochlore is generally tougher than perovskite. The Vickers hardness of a $\text{Gd}_2\text{Ti}_2\text{O}_7$ composition was 10.48 GPa while $(\text{Nd}_{1-x}\text{Yb}_x)_2\text{Zr}_2\text{O}_7$ ranged from 7.5 to 10.5 GPa depending on the dopant level. For comparison the microhardness of $(\text{La}_2(\text{Zr}_{1-x}\text{Ce}_x)_2\text{O}_7)$ ranges from 3.7 to 1.3 GPa [10,11]. The fracture toughness of the $(\text{Nd}_{1-x}\text{Yb}_x)_2\text{Zr}_2\text{O}_7$ was lower than the $(\text{La}_2(\text{Zr}_{1-x}\text{Ce}_x)_2\text{O}_7)$ by about 0.33 $\text{MPa m}^{1/2}$ likely due to the lower $(\text{La}_2(\text{Zr}_{1-x}\text{Ce}_x)_2\text{O}_7)$ hardness [10,12]. Interestingly the intermediate composition of $(\text{La}_2(\text{Zr}_{1-x}\text{Ce}_x)_2\text{O}_7)$ is composed of both the pyrochlore and fluorite structures samples and had the highest fracture toughness. The fracture toughness can be attributed to the thermal expansion coefficient mismatch between the pyrochlore and fluorite structures that contributes to induced internal stress [12]. A comparison of the hardness and toughness of pyrochlore and perovskite is given in Fig. 8.2.

Radiation damage also has a softening effect on the fracture toughness of brittle materials, specifically pyrochlores [13]. An increase in dose leads to toughening then further irradiation leads to relaxation. This is due to a mechanical mismatch between irradiated regions and pristine regions leading to an increase in internal stress. This effect and other effects of radiation damage will be discussed further in Section 4.

Table 8.1 The Young's modulus, Vickers hardness, and fracture toughness of some of the phases in SYNROC are given.

Phase	Youngs modulus	Vickers hardness	Fracture toughness	References
Perovskite	154–200	8.4–9.7	0.85–1.2	[1–3]
Pyrochlore		7.5–10.5	1.27–3.8	[6–8]

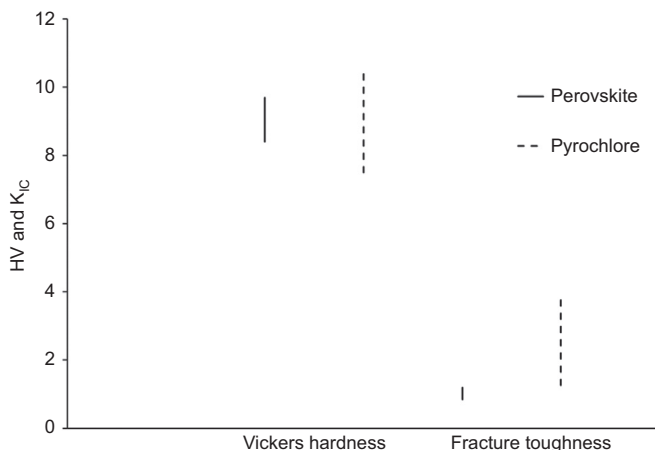


Figure 8.2 Mechanical properties of some of the SYNROC phases [6–8,11–13].

8.3 Corrosion/leaching studies of candidate single-phase and multiphase materials

8.3.1 Corrosion and leaching techniques

Since the 1980s several techniques have been developed to measure the durability of glass waste forms. Many of these techniques are also applicable to ceramic waste forms. Some of the more well-known methods of measuring elemental leaching in ceramic waste forms are the ASTM C 1285 product consistency test (PCT) and the ASTM C 1220 (MCC-1) monolithic specimen test. In Fig. 8.3, a diagram of the PCT, MCC-1, and vapor hydration tests (VHT) is given. Both of the PCT and MCC-1 tests submerge the sample in DI water at a specific pH and temperature. Then, a small amount of solution is extracted after a given time, and inductively coupled plasma mass spectrometry (ICP-MS) is performed to measure the elemental composition of the water. The PCT and monolith methods have been used to create benchmarks for waste performance and are currently used at waste processing plants. Alternatively, the VHT experiment is used to develop reacted surface layers to study.

8.3.2 PCT product characterization test

The PCT is a method to examine the quantitative dissolution of elements over time [14,15]. The samples are typically crushed into a fine powder, with known particle size. The powders are then placed inside a 304L stainless steel reaction vessel filled with demineralized water.

There are a standard PCT-A and a nonstandard PCT-B test. PCT-A is performed specifically at 90°C for exactly 7 days with a water/sample mass ratio of 10:1, while the PCT-B test has no set time, temperature, or any other controlled variables [14].

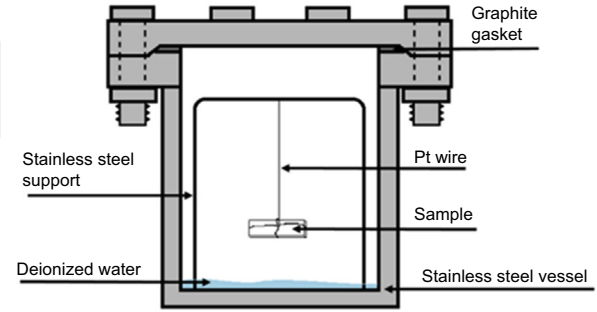
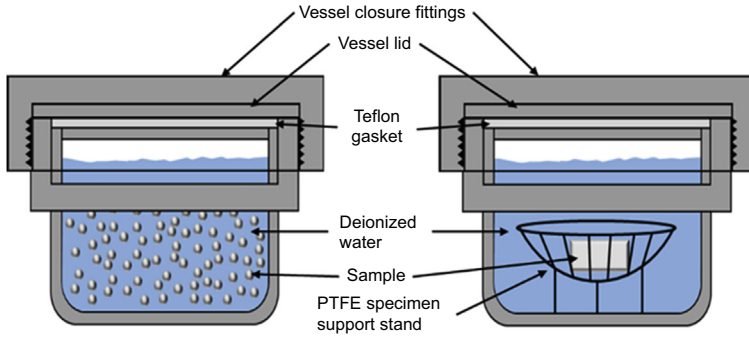


Figure 8.3 Diagrams for the PCT, MCC-1, and VHT experiment setup.

Once the tests are completed, the leachate is collected and analyzed using ICP-MS. The purpose of the PCT test is to measure the chemical durability of waste forms in carefully controlled conditions.

8.3.3 MCC-1 monolith test

The monolithic leach test, or ASTM C 1220, is performed on sample monoliths or chunks with a chosen surface area to volume ratio [16]. In addition to the samples, two blanks and a standard reference material, called as the approved reference material, are prepared in addition. The samples and standards are loaded into seal stainless steel pressure vessels filled with deionized water and heated at $\sim 90^{\circ}\text{C}$ for ~ 7 days. The vessel is then cooled and the leachates are filtered, acidified, and the elemental composition is measured by ICP-MS. The concentration of elements in the leachates is compared to the elemental concentrations in the unleached samples to obtain a fraction loss for each element. Generally, the monolith test is run in triplicate to filter out effects from sample inhomogeneities. The purpose of the monolith test is to measure the chemical durability of waste forms under low surface area to leachant volume conditions. The monolith tests allows for grain boundary and surface effects that are not captured by the PCT test.

8.3.4 Vapor hydration test

Vapor hydration test (VHT) is a method to study the corrosion and alteration of waste glass and ceramic materials by simulating the humid environment where waste forms are stored [17–19]. Monolithic samples are suspended inside a 304-L stainless steel vessel. The sample is suspended by a platinum wire that is tied to stainless steel stand inside the vessel. To achieve 100% humidity inside the reaction vessel, a calculated amount of water is added, depending on the volume of the vessel and testing temperature. The amount of water does not affect the rate of alteration [19]. Due to the high humidity, inside of the chamber, a thin layer of water will condense on the surface of the samples allowing for aqueous leaching to occur and the formation of an alteration layer on the surface.

There are no standard times or temperatures for VHT. Experiments have been carried out up to 7 years and anywhere from 40 to 300°C [17,20]. The purpose of VHT is to generate larger alteration layers and secondary phase formation to gain knowledge of the long-term corrosion processes of waste forms.

8.3.5 Corrosion studies of glass waste forms

Corrosion of glass waste forms involves the surface of glass dissolving and forming an amorphous hydrated gel, called an alteration layer. There are four stages of glass corrosion that form the alteration layers [18,19,21]. The first stage involves glass reactive with the dilute solution at a constant rate. The second stage of reaction occurs when the alteration product concentration is high enough to limit the reaction rate. The third stage occurs when the alteration products start to nucleate and grow. The fourth stage

of alteration is identified when the alteration becomes constant again [19]. Leaching experiments at various temperatures and times have shown that engineered glass produces similar alteration products as natural glass [18,19,21]. In comparison to the VHT testing of zirconolite rich SYNROC, waste glasses examined after VHT typically exhibited a larger alteration area in a less amount of time and an initial dissolution rate of about $1 \text{ g/m}^2/\text{d}$ [22,23].

Glass-ceramic composites have also been developed to enable higher loading and better retention of specific radionuclides of ceramic phases while maintaining the compositional flexibility of glass [24–26]. In a study by Crum et al. PCT-B testing was used to examine Cs leaching on glass-ceramic composites for 3 and 28 days [25]. The three glass-ceramic composites had varying compositions but similar leach rates. Although Cs showed preferential partitioning into the glass phase of the multiphase structure, the leached concentrations were similar to single-phase waste glass [25].

8.3.6 Corrosion studies of multiphase waste forms

8.3.6.1 SYNROC type waste forms C

The component phases for the SYNROC type waste form assemblage have been studied since the 1980s. A significant amount of studies have focused on the chemical durability to aqueous leaching of these phases both separately and together. When Cs is present it is often used to measure leaching, as it has high water activity [27–33]. For waste forms containing highly active ions, such as Cs, structural and chemical analysis of the system is very important. In the case of Cs and Mo containing waste forms, a preferential Cs–Mo secondary phase is likely to form due to their affinity if they are not immobilized in separate durable phases. Owing to the high aqueous solubility of Cs–Mo formulations, waste forms containing these phases exhibit poor aqueous durability. This result has encouraged the development of Cs-containing hollandites that are durable and compatible with a melt and crystallization process [34–36].

SYNROC C and SYNROC D both have the capacity to immobilize the waste stream elements in multiphase ceramic agglomerations. SYNROC D is composed of the zirconolite, perovskite, pyrochlore, and nepheline phases, while SYNROC C is composed of zirconolite, perovskite, pyrochlore, and hollandite phases. In general, the leaching durability of SYNROC phases from the highest to the lowest is zirconolite (C,D), then perovskite(C,D) and pyrochlore (C,D) (spinel), and then hollandite (C), pollucites, nepheline (D) [32].

A difficulty with developing multiphase waste forms is understanding the interactions between the phases and emerging secondary phases. Controlling the secondary phases is especially important in leaching as secondary phases typically have poorer leaching resistance than the parent phase [37]. The surface alteration layer of Pu-bearing zirconolite-rich SYNROC was measured by TEM and showed a 100–200 nm thick alteration layer on the surface of the ceramic. The formation of this layer was believed to have resulted from the dissolution of some secondary phases. This seems reasonable as the parent zirconolite phases exhibited no corrosion

and there was an iron-rich Pu containing precipitates on the zirconolite. Although the zirconolite parent phase exhibited no corrosive indicators, the presence of a parasitic secondary phase leads to unexpected increases in leaching rates and should be considered when planning waste form compositions.

SYNROC samples are more resistant to leaching than borosilicate glass waste forms [21]. However, as there are no benchmark or ASTM standards for ceramic waste forms and the dissolution mechanisms and processes are different, it is difficult to directly compare the two different waste form systems. Additionally, the dissolution mechanisms for SYNROC is less well defined compared to borosilicate waste forms.

8.3.7 Corrosion studies of single-phase waste forms

8.3.7.1 Zirconolite and pyrochlore

The structures of zirconolite and pyrochlore are similar. Owing to mutual ion substitution, both phases have to be considered when determining solubility limits and phase formation for waste form planning [38–40]. These two phases can immobilize the M^{3+} and M^{4+} actinides present in the waste stream. The initial leaching rate from these phases is on the order of 10^{-2} g/m²/d while the long-term leaching rate is 10^{-5} to 10^{-6} g/m²/d [38,41–44].

Several factors contribute to the dissolution rate. First being the immobilized species, for example, Ca versus Nd, but also temperature, pH, and surface alteration (via dissolution or by radiation damage) can have a factor. For zirconolite and zirconolite-pyrochlore systems, higher temperatures lead to faster alteration of the surface layer as seen in a study of $(Ca_{0.8}Nd_{0.2})(ZrTi_{1.8}Al_{0.2})O_7$ at 100 and 200°C [41]. Ionic diffusion can be slowed by the surface alteration layer. This feature of leaching has been shown in several studies and is sometimes avoided by prewashing the samples in DI water. By washing the initial leaching rate is bypassed and the long-term leaching rate is more rapidly acquired [38,41–44].

The pyrochlore structure behaves similar to zirconolite in terms of leaching rates. In a study of a series of $Ca_{1-x}Zr_{1-x}Gd_{2x}Ti_2O_7$ samples regardless of the formed structure the normalized release rate were all normalized leach rates were low on the order of 10^{-6} to 10^{-8} g/m²/day [38]. Additionally, when pyrochlore is compared to brannerite (UTi_2O_6), another U immobilizing waste form, pyrochlore, is found to be superior in terms of leach resistance, $\sim 10^{-5}$ [45].

Radiation damage does effect the leach resistance of structures, primarily when the structure undergoes a structural amorphization. This is due to a disruption of the order structure that is providing a favorable environment for the target ions. The leaching of Cu and Pu from $Gd_2Ti_2O_7$ and $GdZrTi_2O_7$ pyrochlore systems is normally on the order of 0.01 and 0.12 g/m². After radiation-induced amorphization, the leach rate increased by 10–50 times [46].

8.3.7.2 Perovskite

Leaching of the perovskite is slightly worse than zirconolite and pyrochlore [47]. Generally, the lighter rare earth elements such as Ce and Nd partition into perovskite.

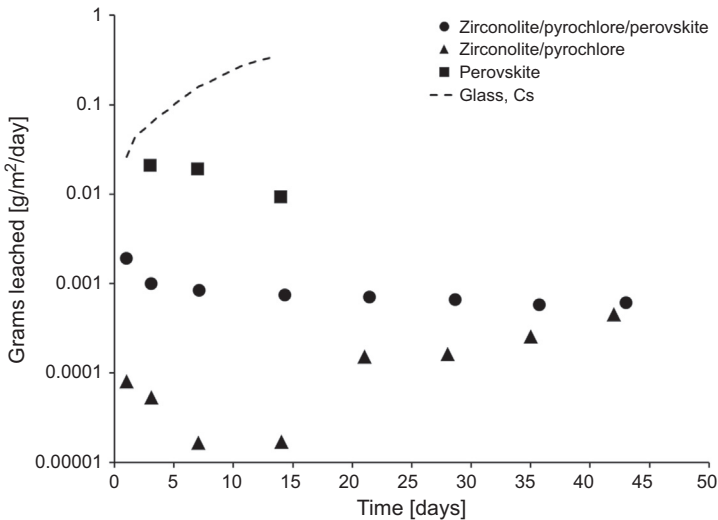


Figure 8.4 Nd leaching from zirconolite and mixed zirconolite/pyrochlore/perovskite waste forms [44,48,49].

Fig. 8.4 shows the trend of Nd leaching for different zirconolite, perovskite, and pyrochlore composites. Samples containing perovskite generally exhibit poorer Nd leaching compared to zirconolite and pyrochlore. When comparing zirconolite, pyrochlore, and perovskite composites, the Nd leaching was slightly high than similar composites not containing perovskite. It was noted that this result was likely due to the partial incorporation of Nd into the perovskite phase that has poorer relative leaching. The Nd leaching was still lower than SYNROC and borosilicate glass leaching [48,49].

8.3.7.3 Hollandite

Articles discuss hollandite leaching [22,28–31,50–59]; Hollandite leach resistance is two orders of magnitude lower than current glass waste forms [28]. The leaching rate or amount of release ions varies some with the composition and is mostly independent of surface area and as reported by Fillet et al. about 4×10^{-2} g/m²/d [31,41].

Carter et al. performed PCT-B testing on single-phase hollandites [28]. As is characteristic of leaching from ceramics during the initial few days the leaching rate spikes and quickly drops off, which is sometimes avoided by prewashing the hollandite with DI water. Carter showed that at longer leaching times, 84–128 days, the release rate decreased by two orders of magnitude compared to the 7-day tests. Additionally, they found that Ba and Cs leach congruently and after 56 days the normalized leach rate was <0.001 g/m²/day, which is similar to other reported results [28,30,54]. Some of these results have been given in Fig. 8.5.

For the most part, the effect of pH on leaching is inconsequential. However, below pH = 1 the release of Cs and Ba from the hollandite structure is accelerated by a factor

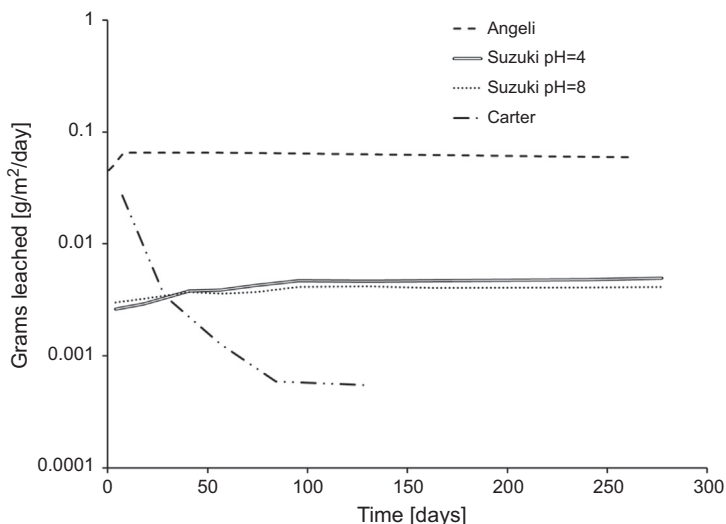


Figure 8.5 Cesium leaching from hollandite waste forms.

Data from M.L. Carter, E.R. Vance, D.R.G. Mitchell, J. V Hanna, Z. Zhang, E. Loi, Fabrication, characterization, and leach testing of hollandite, (Ba, Cs) (Al, Ti)₂ Ti₆ O₁₆, *J. Mater. Res.* 17 (October 2002); T. Suzuki-Muresan, J. Vandenborre, A. Abdelouas, B. Grambow, S. Utsunomiya, Studies of (Cs,Ba)-hollandite dissolution under gamma irradiation at 95°C and at pH 2.5, 4.4 and 8.6, *J. Nucl. Mater.* 419 (1–3) (2011) 281–290; F. Angeli, P. McGlinn, P. Frugier, Chemical durability of hollandite ceramic for conditioning cesium, *J. Nucl. Mater.* 380 (2008) (1–3) 59–69.

of 10 due to the reactive surface being completely altered to rutile [31]. Additionally, most studies found that there are no solubility constraints on Ba and Cs leaching as the surface area, or more specifically the SA/V ratio, had little to no effect on the leaching rate [31]. In the same way, subsurface damage by mechanical polishing does not affect the leaching rate of Ba and Cs from hollandite either [52].

Radiation damage can have an impact on elemental leaching. In heavy-ion radiation experiments by Grote et al., the elemental release of Cs ions nearly doubled after being exposed to a sufficient dose to cause radiation-induced amorphization [50]. It was suggested that the amorphization leads to a collapse of the tunnel allowing for easier Cs diffusion. γ - and β -radiation have significantly less effect on elemental leaching [30,54,57].

8.3.8 Uranium dioxide

The potential use of spent UO₂ fuel as a direct storage media from light water reactors has prompted developing of an understanding of the leaching behavior and leaching mechanism for UO₂ [60,61]. High burnup UO₂ fuel has been shown to develop a porous outer ring that can severely impact the leaching rate, due to the outer rings high porosity and grain subdivision, that is, smaller grain size [60]. Although UO₂

does not become amorphous high concentrations of fission products or high damage lead to grain subdivision that is undesirable. If the damage is high enough to lead to grain subdivision, the leaching rate, or rather surface oxidation rate, increases.

8.4 Radiation effects on surface, mechanical properties, and leaching

8.4.1 Radiation damage processes

For a waste form to be functional, a certain resistance to radiation-induced damage is necessary to the decay of the incorporated of radioactive nuclides. There have been several studies looking at the effect of radiation on ceramic waste forms. To investigate the durability of ceramic waste forms, studies using radioactive bearing phases and experiments using electron, neutron, γ , and accelerated heavy ions have been performed [54,62–66]. For example, Kr^{2+} ions have been used to simulate α -damage of constituent SYNROC phases, hollandite, zirconolite, and perovskite [24,67]. Radionuclide decay affects crystalline materials through the interactions of the emitted β -particles, α -particles, recoil nuclei, and γ -rays with the waste form material. These interactions fall into two categories: the transfer of energy to electrons, by ionization and excitation reactions, and by the transfer of energy to nuclei, by ballistic two-body collisions, as illustrated in Fig. 8.6 [68]. For β -particles and γ -radiation, the energy transfer process is dominated by ionization processes, leading to electronic defects. However, the energy transfer process for α -particles and recoil nuclei involves ionization and elastic collisions, forming electronic and atomic defects. The energy loss of α -particles is attributed primarily to ionization processes, while recoil nuclei primarily lose energy by elastic collisions. The average energy absorbed by ionization and electronic excitation is similar for ceramic waste forms and glass waste forms [69,70]. The resulting micro- and macrostructural changes (volume swelling, structural transformations, and crystalline-to-amorphous transition) resulting from radiation damage can lead to increased leaching rates [65]. Therefore, understanding and developing radiation-resistant materials is important for responsibly disposing of nuclear waste.

8.4.2 Radiation damage process for crystalline structures

8.4.2.1 Frenkel pair defects

Frenkel pair defect is a point defect consisting of a vacancy and interstitial defect pair. It is formed when a lattice ion is displaced from its site, forming a vacancy, and the displaced ion comes to rest at an unoccupied lattice site or interstitial site. The displacement of lattice atoms in ceramic materials generally requires between 20 and 80 eV [71,72]. This is called the threshold displacement energy, E_d , which is the minimum required kinetic energy for atom displacement. Structural amorphization is a result of the accumulation of simple Frenkel defects and amorphous, or aperiodic,

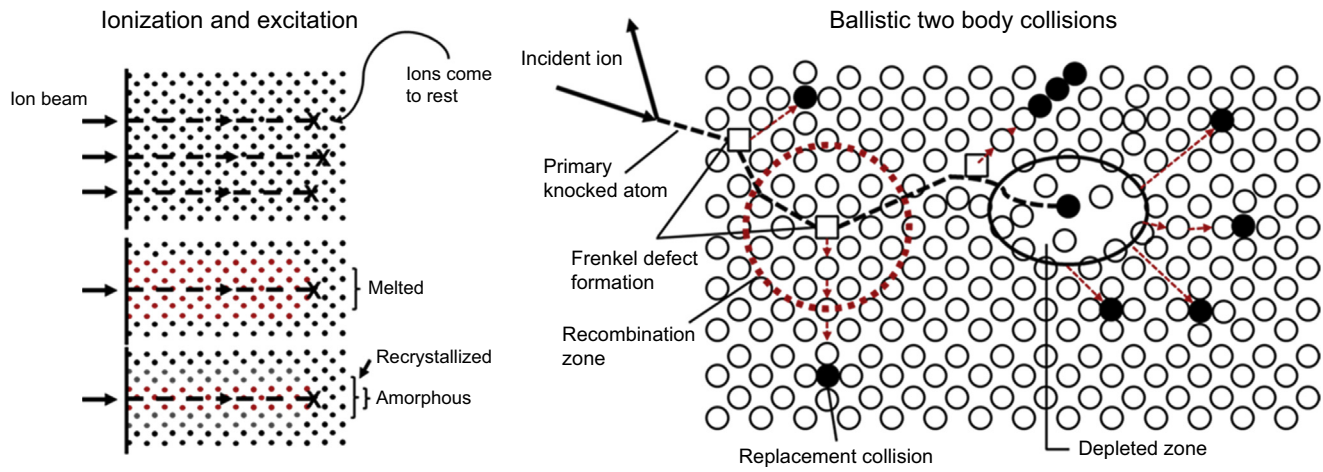


Figure 8.6 Left: Melting and epitaxial recrystallization due to ionization energy transfer. Right: Illustration of atomic displacements caused by incident α -particles.

Modified from Olander Fig. 17.20 and 17.25 D.R. Olander, Fundamental Aspects of Nuclear Reactor Fuel Elements, 1976.

regions generated from α -decay events. The accumulation of these defects and resulting amorphous regions are characteristic of the loss of long-range order [73,74]. Atomic displacement is primarily caused by α -particle and recoil nucleus radiation as they have the necessary energy to displace a lattice ion.

8.4.2.2 *Electronic defects*

Electronic defects form through ionization and excitation reactions produced from α -particles, β -particles, and γ -rays. The most significant energy loss mechanism for β -particles and α -particles is via coulombic interactions. Similarly, γ -rays lose most of their energy through photoelectric effect interactions via Compton scattering and electron–positron pair production. The ionization and excitations created from these particles and rays produce a large number of electron–hole pairs [69,75–77].

Some examples of electron–hole pair defect formation that have been reported for hollandite are paramagnetic defects [62]. The first is a hole center due to a superoxide ion O_2^- resulting from hole trapping by interstitial oxygen. The second, an electron center is formed where Ti^{4+} captures an electron, becomes Ti^{3+} , and is adjacent to an oxygen vacancy. The third, an electron center formed where Ti^{4+} captures an electron, becomes Ti^{3+} , and is adjacent to an extra Ba^{2+} , the extra Ba^{2+} arose from barium displacement by elastic collision [62,78]. Electron irradiations have been shown to simulate β -particle and γ -ray Compton electron defect formation [69,77].

8.4.2.3 *Volume change*

Waste forms exposed to radiation undergo volume change induced by defect formation. The volume change can be attributed to structural changes in the crystalline phase, formation of secondary phases, void or defect agglomeration, and amorphization. In glass waste forms, depending on the type of radiation, the volume can increase or decrease. In some cases, volume expansion of 50% has been observed under electron radiation [70,79]. In ceramic waste forms, volume expansion can be as much as 20% depending on the phase [70]. The swelling of SYNROC C is typically about 6%–7%, which is greater than the swelling of its constituent phases, given in Fig. 8.7, but this can vary depending on the composition [69,70,80]. Most of the volume change for glass and ceramic waste forms occurs before amorphization at radiation doses below the critical amorphization dose [75,81–83].

8.4.2.4 *Crystalline long-range order amorphization*

Amorphization of ceramic waste forms is an important topic as most ceramic waste form materials experience a structural change upon irradiation that is typically a crystalline-to-amorphous transformation and results in increased leaching of the irradiated material [5,50]. The onset of amorphization is typically described as the dose required to form an identifiable halo in the SAED pattern. This indicates the long-range order of the structure is becoming disrupted. The critical amorphization dose is the dose required for the structure to be fully amorphous, which can be identified by having no residual crystalline pattern in the selected area electron diffraction

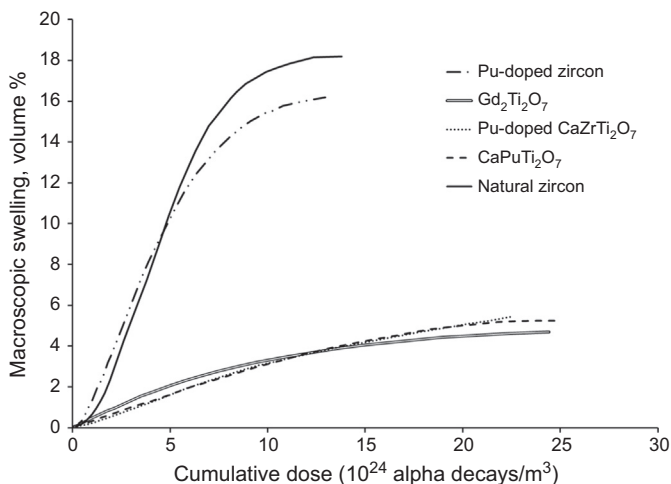


Figure 8.7 Natural zircon [74], Pu-doped zircon [82], Pu-doped $CaZrTi_2O_7$ [46], $CaPuTi_2O_7$ [46], $Gd_2Ti_2O_7$ [70].

(SAED) image. The dose for these two benchmarks primarily depends on the structure, for example, zirconolite and hollandite, and secondarily depends on the composition.

Although the process of amorphization is not precisely defined, the amorphization of the ceramic waste form materials has been shown to occur heterogeneously by either: an α -recoil displacement cascade, an overlap of α -recoil cascades reaching a sufficiently high concentration, or a combination of the two phenomena. Amorphization leads to an aperiodic structure that often is coupled with a significant volume change [65].

The amorphization process is initiated by a damage cascade where the incident particle in-elastically collides with lattice atoms. These collisions transfer momentum and heat, which lead to melting and secondary defect formation in the cascade zone [65,84]. All crystallinity in this cascade zone is disturbed; then, some fraction is recrystallized via epitaxial recrystallization from the surrounding intact structure. If recrystallization is incomplete, then an amorphous region forms that will accumulate upon subsequent irradiation. The final crystal structure depends on the initial structure chemistry, temperature, as well as the irradiation parameters.

In the case of electron irradiation of hollandites, the electronic defects formed from this irradiation typically do not recombine upon annealing and some, such as Ti^{3+} and O^{2-} , migrate to form defect clusters [62,77].

When exposed to heavy ion irradiation, such as Ar^+ , Kr^{2+} , or Ne^{2+} , the inclusion of heavy ions and interruption of the unit cell structure can lead to structural distortion and amorphization [50,73,85]. Annealing is effective in some circumstances as studies of the amorphization behavior of pyrochlore and hollandite have been performed at elevated temperatures to show the defect recovery behavior of ceramics [82–84]. As with most materials, at elevated temperatures, ceramic waste form materials have a critical amorphization temperature at which the annealing kinetics outweigh

the damage kinetics and full recrystallization occurs within the cascade zone. Materials are highly resistant to radiation damage when above the critical amorphization temperature. The critical amorphization temperature varies between materials, from 200 to 1200°C, and is a useful property to consider when developing an effective waste form [50,82,83,86]. Fig. 8.8 shows the transition of pristine hollandite to the fully amorphous structure and the structure change that MgIn_2O_4 , an inverse spinel, to a rock salt-like structure.

One way to improve the radiation tolerance of materials is by processing the material in such a way to produce a nanocrystalline microstructure. It has been shown in

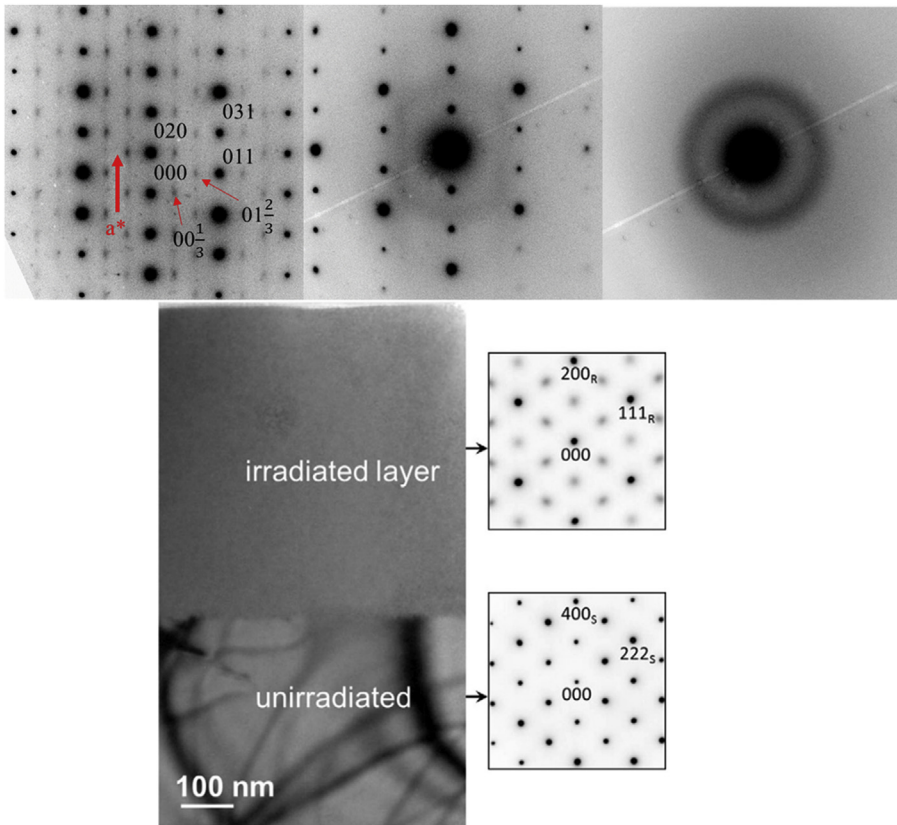


Figure 8.8 SAED micrographs pristine, the onset of amorphization, and full amorphization of hollandite and the pristine, intermediate to amorphous phase transitions for MgIn_2O_4 .

Figures from R. Grote, T. Hong, L. Shuller-Nickles, J. Amoroso, M. Tang, K.S. Brinkman, Radiation tolerant ceramics for nuclear waste immobilization: structure and stability of cesium containing hollandite of the form $(\text{Ba,Cs})_{1.33}(\text{Zn,Ti})_8\text{O}_{16}$ and $(\text{Ba,Cs})_{1.33}(\text{Ga,Ti})_8\text{O}_{16}$, *J. Nucl. Mater.* 518 (2019) 166–176; M. Tang, J.A. Valdez, Y. Wang, J. Zhang, B.P. Uberuaga, K.E. Sickafus, Ion irradiation-induced crystal structure changes in inverse spinel MgIn_2O_4 , *Scripta Mater.*, 125 (2016) 10–14.

several studies that bulk and nanocrystalline structures have different responses [88–92]. This behavior is believed to be driven by the more rapid annihilation of ion-induced defects in nanocrystalline structure due to the larger amount of grain boundaries [93]. Additionally, structural ordering can play a role in improving radiation tolerance. This behavior has been shown by a pyrochlore waste form composition. The crystalline and composition were the same; however, the degree of disordering was different [93].

8.4.3 Radiation induced surface damage

The depth of the surface layer for a ceramic exposed to radiation is dependent on the ionizing energy and material composition. However, radiation damage can lead to amorphization, volume expansion, and microcracking (or fracturing) in the near surface that greatly increases the microstructure complexity [69,70,73,82,94]. Additionally, the analysis of the surface layer can be difficult due to the thinness of the layer, which is generally only a few hundred nanometers thick. Techniques such as cross-sectional TEM and grazing incidence X-ray diffraction can be useful for characterizing the crystalline structure of these thin regions [50].

8.4.3.1 Amorphization

The entire volume of a radionuclide bearing material will be subjected to the radiation dose. However, in the case of multiphase waste forms such as SYNROC C, this assumption is not entirely valid. Phases, such as hollandite, which do not contain α -emitting isotopes, will suffer radiation damage only on the surface. The penetration depth of the damaged layer depends on the ion energy and material composition. Studies on waste form ceramics have shown that the crystalline structure can become amorphous when exposed to α -irradiation [49]. In the case of Pb^{3+} ion bombardment, at a dose of 3×10^{14} ions/cm [2], the crystalline structure of zirconolite becomes fully amorphous to a depth of 100 nm [41]. Similarly, the surface of the hollandite will become amorphous when exposed to Kr^{2+} ion bombardment. At a dose of $1.5\text{--}3.9 \times 10^{14}$ ions/cm² (depending on the composition), the hollandite surface will become fully amorphous to a depth of 250 nm [50].

8.4.3.2 The effect of volume expansion on the surface

Amorphization can lead to macroscopic changes such as surface cracking and swelling of the surface layer. Additionally, macroscopic changes can be caused by the accumulation of point defects, emergent phases, and the growth of microstructural defects (voids, gas bubbles, and dislocations) [13,69]. At the smallest scale, point defects lead to unit cell volume change. These volume changes can be propagated up the length scales and result in cracking due to either residual stress or void agglomeration. Cracking has also been shown to occur if the concentration of bubbles reaches and critical threshold [68,69].

8.4.3.3 How radiation effects mechanical properties

For both metals and ceramics, ion implantation has been used to change the mechanical properties of the surface of a material. The effect of amorphization on hardness, elastic modulus, and fracture toughness has been investigated for several ceramic phases using radioactive isotopes and heavy-ion irradiation [13,46,69,95]. Under α -irradiation, the microstructure consists of individual amorphous tracks following the path of the high energy α -recoil particles and fission fragments. At low doses, the microstructure could be described as a composite crystalline-amorphous structure in which the internal strain between phases prevents crack propagation and increases fracture toughness [13,46,95]. At a higher dose, the amorphous phase becomes dominant with residual dispersed crystallites. The fracture toughness decreases as the internal stored energy is reduced [69,95,96]. The effect of radiation on fracture toughness can be seen in Fig. 8.9.

The result α -decay on crystalline ceramics is that the fracture toughness is increased due to a softening of the hardness and reduction of the elastic modulus. This property change makes α -irradiated ceramic waste forms more resistant to crack propagation.

8.4.3.4 How radiation effects leaching

Depending on the phase, radiation damage can have a significant effect on the leach rate. For example, hollandite is highly resistant to ionizing radiation, β -particles, and γ -rays, as experimentally determined by electron irradiation experiments [54,98].

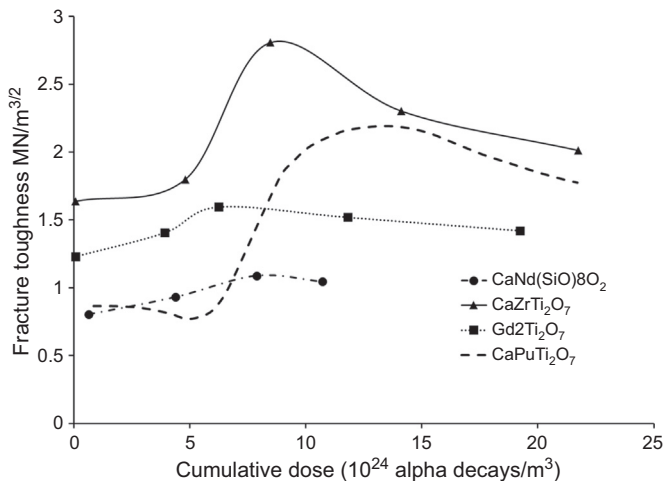


Figure 8.9 Softening and hardening effect on fracture toughness due to radiation damage. Data from W.J. Weber, H. Matzke, Effects of radiation on microstructure and fracture properties in $\text{Ca}_2\text{Nd}_8(\text{SiO}_4)_6\text{O}_2$, Mater. Lett. 5 (1–2) (1986) 9–16; W.J. Weber, J.W. Wald, H. Matzke, Effects of self-radiation damage in Cm-doped $\text{Gd}_2\text{Ti}_2\text{O}_7$ and $\text{CaZrTi}_2\text{O}_7$, J. Nucl. Mater. 138 (2–3) (1986) 196–209; F.W. Clinard, D.S. Tucker, G.F. Hurley, C.D. Kise, Scientific basis for nuclear waste management VIII, Mater. Res. Soc. 663 (1986).

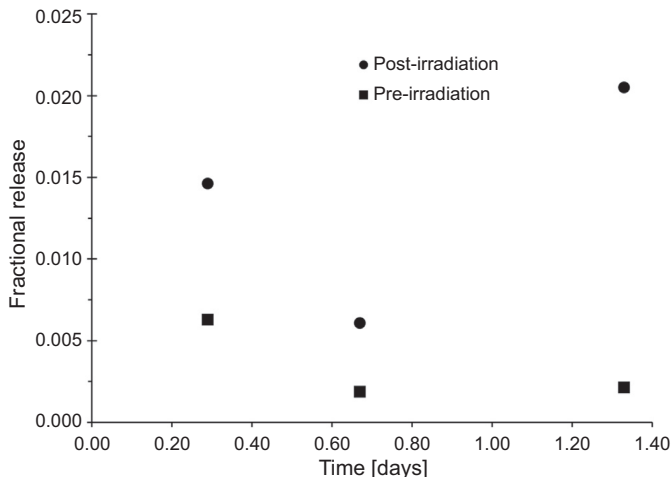


Figure 8.10 Elemental leaching of hollandite increased after α -irradiation-induced amorphization.

Data from R. Grote, T. Hong, L. Shuller-Nickles, J. Amoroso, M. Tang, K.S. Brinkman, Radiation tolerant ceramics for nuclear waste immobilization: structure and stability of cesium containing hollandite of the form $(\text{Ba,Cs})_{1.33}(\text{Zn,Ti})_8\text{O}_{16}$ and $(\text{Ba,Cs})_{1.33}(\text{Ga,Ti})_8\text{O}_{16}$, *J. Nucl. Mater.* 518 (2019) 166–176.

Although there is significant electronic defect formation, leaching experiments of γ -irradiated hollandite show that these defects are insignificant to the leaching resistance [54]. However, α -irradiation does have a negative effect on the leaching resistance of hollandite after irradiation as illustrated in Fig. 8.10 [50]. The leach rate of pristine hollandite is similar to the durable zirconolite actinide waste form and slower than other Cs containing phases such as Cs-pollucite and Cs-silicotitanates [41,54]. It has been noted that in glass waste forms, radiation-induced swelling and amorphization lead to a leaching increase of nonnetwork ions by a factor of 10–50 [46]. A similar effect of increased leaching rate has been noted for some waste forms, including hollandite, when radiation-induced swelling and amorphization occurs [46,50,60,99,100].

However, exposure to radiation causes negative changes in the properties of waste form materials. The durability of ceramic waste forms is competitive and in some cases superior to other waste form options.

8.5 Morphology drivers for irreversible species diffusion and transport in HeteroFoams

8.5.1 Flux of an included species

Consider the storage of Cs waste material in a heterogeneous medium, specifically, a Hollandite structure with morphology as shown in Fig. 8.11. The question addressed

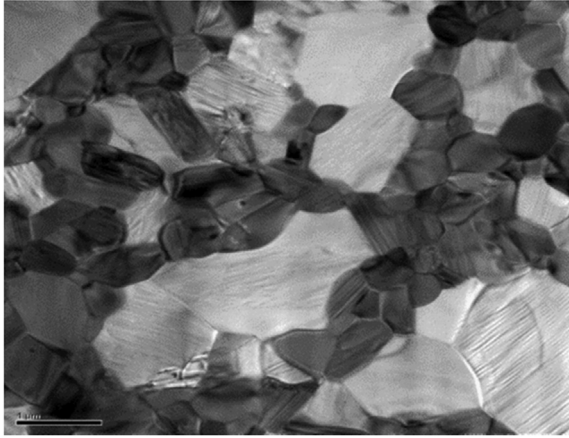


Figure 8.11 Heterogeneous morphology of a hollandite- $\text{Nd}_2\text{Ti}_2\text{O}_7$ waste form material made by Brinkman et al. [101,102] material [10].

here is the effect morphology has on the effectiveness over time of the storage medium to keep the radioactive material from escaping to the surroundings. To be most effective, should the storage phase be a single mass surrounded by the second phase or finely divided into a distributed phase? A detailed discussion of the problem in its entirety is found in Ref. [101]. An outline of that discussion serves our present purposes.

The following discussion on the effect of morphology will use the Nernst–Plank relationship, as presented below.

$$N_i = -D_i \nabla c_i - z_i u_{m,i} F c_i \nabla \phi + c_i u \quad (8.1)$$

N_i = flux of species, i ($\text{mol}/\text{m}^2 \cdot \text{s}$)

D_i = flux of species, i (m^2/s)

z_i = valance of species

c_i = flux of species, i (mol/m^3)

The first necessary assumption is that there is no fluid flow present within the geometry so that the velocity term u_i is ignored, and the second is that there is no electrical potential applied over the boundaries so that the migration term becomes zero.

Therefore, here the leaching of Cesium ions will primarily take place by the diffusion of the waste species present in the waste form. Therefore, the focus is on the effect of morphology due to the diffusion from distributed phases in HeteroFoams. The problem is set on the following effective volume model.

Flux is calculated using a discrete element method set on the actual microstructure rendered by W. Chiu from micro-X-ray images of actual waste form materials. In addition, certain idealized microstructures (such as the spheres with different sizes

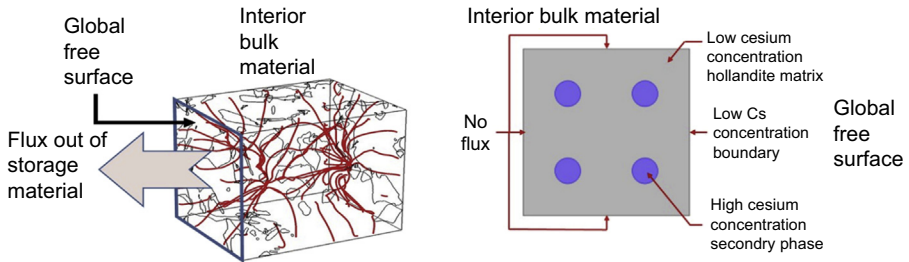


Figure 8.12 Calculated flux paths of Cs ions from the bulk center toward the boundaries through a hollandite waste form structure.

shown in the right of Fig. 8.12) were used to study the principles controlling the flux out of the waste form with time. Only the 2-D results will be considered here, with very little loss of generality. Some conclusions can be drawn from a comparison of the number of inclusions to the boundary flux at various times, initial, 10 days, 100 days. For a given volume fraction of stored waste, dividing the stored material into smaller pieces (i.e., finer microstructure) results in larger surface to volume ratios causing more exit flux in the early stages of storage, but surprisingly, less total loss in the later stages of storage. The concentration in the smaller particles is reduced earlier making the average concentration gradient slope that “pushes” the flux smaller over time. The analysis revealed a surprising result that this and other microstructure properties have a small or negligible effect for volume fractions below about 0.4. Therefore, volume fractions below about 0.4 is a “threshold” of concentration for microstructure effects.

Interestingly, this surface-to-volume ratio versus the history of flux rates carries over to changes in microstructure shape. To study that effect, the elliptical versus circular shapes were considered for the same volume fractions, again as a function of global time, from 0 to 100,000 days. The number of particles was held constant and only the shape was changed. For long periods of time (greater than 10 days in this case), the total flux out was essentially identical. However, the surface-to-volume effect (more surface to volume for the elliptical case) revealed another physical principle. In general, after some days, the local gradients ceases to be the principal driver for diffusion, and the total volume element gradient becomes dominant. This change resulted in slower flux out of the exit surface and a more “stable” rate of exit. The global flux gradient is the principal driver at about 50,000 days for the high surface-to-volume elliptical particles, while it takes until about 100,000 days for the global flux gradient to become the principal driver for the circular/spherical waste form particles. This is a general principle; the higher surface-to-volume microstructures have more “early” loss and earlier stable rates of flux than the lower surface-to-volume cases. However, for this change in shape only, the total long-term loss is the same, or indistinguishably different in the calculations.

Finally, for this element of the study, it is possible to discuss space-filling microstructure effects using Voronoi tessellation to fill the volume element so that it looks more like Fig. 8.11. Fig. 8.13 shows an example of that calculation, comparing flux from a top surface (center) to a bottom surface (right).

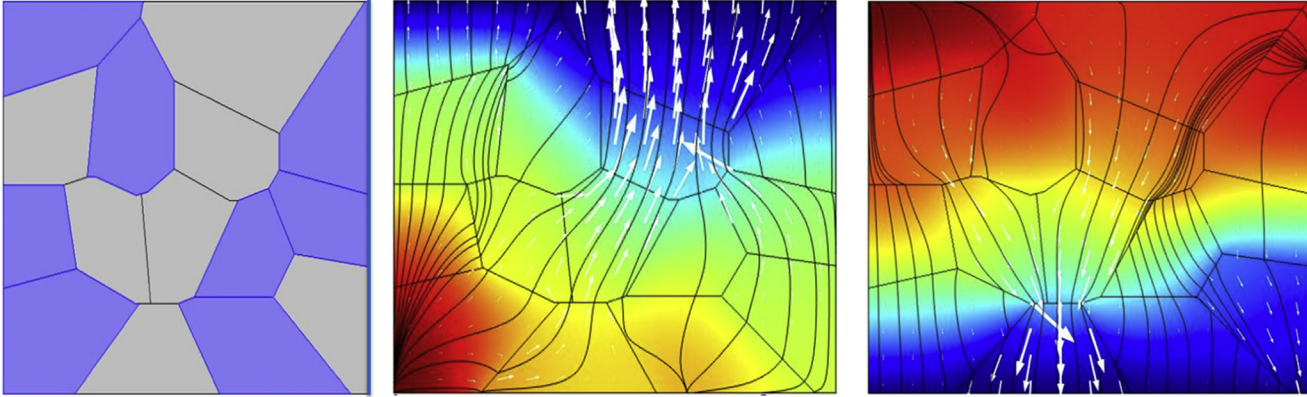


Figure 8.13 Flux from space-filling microstructures generated using Voronoi tessellation showing flux from a top free surface (center) compared to a bottom free surface (right).

The waste storage phase is lighter in tone in that figure, and it is clear that particles near the surface influence very early exit flux, but the global gradient quickly becomes dominant. Therefore, the general principles identified from the idealized shape study seem to remain applicable.

References

- [1] R.C. Ewing, Long term storage of spent nuclear fuel, *Nat. Mater.* 14 (2015) 252–257.
- [2] D. Gombert, P. Steve, T. Trickel, J. Carter, J. Vienna, B. Ebert, G. Matthern, Combined Waste Form Cost Trade Study, 2008 [November 2014].
- [3] C. Biagioni, P. Orlandi, M. Pasero, Ankaungite from the Monte Arsiccio mine (Apuan Alps, Tuscany, Italy): occurrence, crystal structure, and classification problems in cryptomelane group minerals, *Period. Mineral.* 78 (2) (2009) 3–11.
- [4] G.R. Lumpkin, K.P. Hart, P.J. McGlenn, T.E. Payne, R. Giere, C.T. Williams, Retention of actinides in natural pyrochlores and zirconolites, *Radiochim. Acta* 66–67 (1994) 469–474.
- [5] G.R. Lumpkin, R.C. Ewing, Alpha-decay damage in minerals of the pyrochlore group, *Phys. Chem. Miner.* 16 (1) (1988) 2–20.
- [6] X. Hu, X. Cheng, S. Qin, G. Yan, J. Malzbender, W. Qiang, Mechanical and electrochemical properties of cubic and tetragonal, *Ceram. Int.* 44 (2) (2018) 1902–1908.
- [7] Y.-H. Cho, J. Wolfenstine, E. Rangasamy, H. Kim, H. Choe, J. Sakamoto, Mechanical properties of the solid Li-ion conducting electrolyte: $\text{Li}_{0.33}\text{La}_{0.57}\text{TiO}_3$, *J. Mater. Sci.* 47 (16) (2012) 5970–5977.
- [8] K.G. Schell, F. Lemke, E.C. Bucharsky, A. Hintennach, M.J. Hoffmann, Microstructure and mechanical properties of $\text{Li}_{0.33}\text{La}_{0.567}\text{TiO}_3$, *J. Mater. Sci.* 52 (4) (2017) 2232–2240.
- [9] N. Vourdas, E. Marathoni, P.K. Pandis, I. Metallurgie, T.U. Clausthal, Evaluation of LaAlO_3 as top coat material for thermal barrier coatings, *Trans. Nonferrous Metals Soc. China* 28 (8) (2018) 1582–1592.
- [10] Y. Wu, L. Zheng, W. He, J. He, H. Guo, Effects of Yb^{3+} doping on phase structure, thermal conductivity and fracture toughness of $(\text{Nd}_{1-x}\text{Yb}_x)_2\text{Zr}_2\text{O}_7$, *Ceram. Int.* 45 (3) (2019) 3133–3139.
- [11] L. Peng, K. Zhang, D. Yin, J. Wu, S. He, H. He, Self-propagating synthesis, mechanical property and aqueous durability of $\text{Gd}_2\text{Ti}_2\text{O}_7$ pyrochlore, *Ceram. Int.* 42 (16) (2016) 18907–18913.
- [12] W. Ma, X. Li, Y. Yin, H. Dong, Y. Bai, J. Liu, D. Nan, J. Wang, “The mechanical and thermophysical properties of $\text{La}_2(\text{Zr}_{1-x}\text{Ce}_x)_2\text{O}_7$ ceramics, *J. Alloys Compd.* 660 (2016) 85–92.
- [13] W.J. Weber, H. Matzke, Effects of radiation on microstructure and fracture properties in $\text{Ca}_2\text{Nd}_8(\text{SiO}_4)_6$, *Mater. Lett.* 5 (1–2) (1986) 9–16.
- [14] ASTM and C1285-14, Standard test methods for determining chemical durability of nuclear, hazardous, and mixed waste glasses and multiphase glass ceramics: the Product Consistency Test (PCT) 1, ASTM, Conshohocken, USA, 2002 15 (2002) 1–26.
- [15] N.E. Bibler, C.M. Jantzen, “The product consistency test and its role in the waste acceptance process for DWPF glass, *Manag. Radioact. Wastes, Non-Radioactive Wastes Nucl. Facil.* (1989) 743–749.

- [16] ASTM and C1220-10, Standard Test Method for Static Leaching of Monolithic Waste Forms for Disposal of Radioactive Waste vol. 14, December 2010.
- [17] J. Luo, Simulation of natural corrosion by vapor hydration test: seven-year results, *Sci. Basis Nucl. Waste Manag.* XX (465) (1996) 157–163.
- [18] J. Neeway, A. Abdelouas, B. Grambow, S. Schumacher, C. Martin, M. Kogawa, S. Utsunomiya, S. Gin, et al., Vapor hydration of SON68 glass from 90°C to 200°C: a kinetic study and corrosion products investigation, *J. Non-Cryst. Solids* 358 (21) (2012) 2894–2905.
- [19] A. Jiříčka, J.D. Vienna, P. Hrma, D.M. Strachan, The effect of experimental conditions and evaluation techniques on the alteration of low activity glasses by vapor hydration, *J. Non-Cryst. Solids* 292 (1–3) (2001) 25–43.
- [20] T. Kiess, Yucca Mountain project status, *Sci. Basis Nucl. Waste Manag.* XXVI (2003) 3–10.
- [21] J. Neeway, A. Abdelouas, B. Grambow, S. Schumacher, Dissolution mechanism of the SON68 reference nuclear waste glass: new data in dynamic system in silica saturation conditions, *J. Nucl. Mater.* 415 (1) (2011) 31–37.
- [22] D. Harkins, K.S. Brinkman, M.S. Kennedy, F. Peng, The Durability of Single, Dual, and Multiphase Titanate Ceramic Waste Forms for Nuclear Waste Immobilization, 2016.
- [23] D. Caurant, P. Loiseau, O. Majerus, V. Aubin-Chevaldonnet, I. Bardez, A. Quintas, Glasses, Glass-Ceramics and Ceramics for Immobilization of Highly Radioactive Nuclear Wastes, 2009.
- [24] M. Tang, A. Kossoy, G. Jarvinen, J. Crum, L. Turo, B. Riley, K. Brinkman, K. Fox, et al., Radiation stability test on multiphase glass ceramic and crystalline ceramic waste forms, *Nucl. Instrum. Methods Phys. Res. Sect. B Beam Interact. Mater. Atoms* 326 (2014) 293–297.
- [25] J.V. Crum, B.J. Riley, L.R. Turo, M. Tang, A. Kossoy, Summary Report: Glass -Ceramic Waste Forms for Combined Fission Products, Pacific Northwest Natl. Lab., 2011.
- [26] J.V. Crum, L. Turo, B. Riley, M. Tang, A. Kossoy, Multi-phase glass-ceramics as a waste form for combined fission products: alkalis, alkaline earths, lanthanides, and transition metals, *J. Am. Ceram. Soc.* 95 (4) (2012) 1297–1303.
- [27] C.-W. KIM, J.-K. PARK, T.-W. HWANG, Analysis of leaching behavior of simulated LILW glasses by using the MCC-1 test method, *J. Nucl. Sci. Technol.* 48 (7) (2011) 1108–1114.
- [28] M.L. Carter, E.R. Vance, D.R.G. Mitchell, J. V Hanna, Z. Zhang, E. Loi, Fabrication , characterization , and leach testing of hollandite, (Ba, Cs)(Al, Ti)₂Ti₆O₁₆, *J. Mater. Res.* 17 (October 2002).
- [29] A.L. Billings, K.S. Brinkman, K.M. Fox, A.L. Marra, Preliminary Study of Ceramics for Immobilization of Advanced Fuel Cycle, February 2010.
- [30] T. Suzuki-Muresan, J. Vandenborre, A. Abdelouas, B. Grambow, S. Utsunomiya, Studies of (Cs,Ba)-hollandite dissolution under gamma irradiation at 95°C and at pH 2.5, 4.4 and 8.6, *J. Nucl. Mater.* 419 (1–3) (2011) 281–290.
- [31] F. Angeli, P. McGlenn, P. Frugier, Chemical durability of hollandite ceramic for conditioning cesium, *J. Nucl. Mater.* 380 (1–3) (2008) 59–69.
- [32] L.L. Hench, D.E. Clark, J. Campbell, High level waste immobilization forms, *Nucl. Chem. Waste Manag.* 5 (2) (1984) 149–173.
- [33] K.M. Fox, K.S. Brinkman, Development of Crystalline Ceramics for Immobilization of Advanced Fuel Cycle Reprocessing Wastes. Aiken, SC (United States), 2011.
- [34] K.S. Brinkman, K.M. Fox, J.C. Marra, M. Tang, “Crystalline Ceramic Waste Forms: Reference Formulation Report, 2012.

- [35] J. Amoroso, J. Marra, S.D. Conradson, M. Tang, K. Brinkman, Melt processed single phase hollandite waste forms for nuclear waste immobilization: $Ba_{1.0}Cs_{0.3}A_{2.3}Ti_{5.7}O_{16}$; A=Cr, Fe, Al, *J. Alloys Compd.* 584 (2014) 590–599.
- [36] J. Amoroso, J.C. Marra, M. Tang, Y. Lin, F. Chen, D. Su, K.S. Brinkman, Melt processed multiphase ceramic waste forms for nuclear waste immobilization, *J. Nucl. Mater.* 454 (1–3) (2014) 12–21.
- [37] E. Buck, Characterization of a plutonium bearing zirconolite rich synroc.pdf, *Sci. Basis Nucl. Waste Manag.* XX (465) (1997) 1256–1266.
- [38] Y.-B. Zhang, J. Wang, J.-X. Wang, Y. Huang, P. Luo, X.-F. Liang, H.-B. Tan, Phase evolution, microstructure and chemical stability of $Ca_{1-x}Zr_{1-x}Gd_{2x}Ti_2O_7$ ($0.0 \leq x \leq 1.0$) system for immobilizing nuclear waste, *Ceram. Int.* 44 (12) (2018) 13572–13579.
- [39] A.E. Ringwood, S.E. Kesson, N.G. Ware, W. Hibberson, A. Major, Immobilisation of high level nuclear reactor wastes in SYNROC, *Nat. J.* 278 (1979) 219–223.
- [40] R.C. Ewing, W.J. Weber, J. Lian, “Nuclear waste disposal-pyrochlore ($A_2B_2O_7$): nuclear waste form for the immobilization of plutonium and ‘minor’ actinides, *J. Appl. Phys.* 95 (11 I) (2004) 5949–5971.
- [41] C. Fillet, T. Advocat, F. Bart, G. Leturcq, H. Rabiller, Titanate-based ceramics for separated long-lived radionuclides, *Compt. Rendus Chem.* 7 (12) (2004) 1165–1172.
- [42] K. Zhang, D. Yin, K. Xu, H. Zhang, Self-Propagating synthesis and characterization studies of Gd-bearing Hf-zirconolite ceramic waste forms, *Materials* 12 (1) (2019) 178.
- [43] K. Zhang, D. Yin, L. Peng, J. Wu, Self-propagating synthesis and CeO_2 immobilization of zirconolite-rich composites using CuO as the oxidant, *Ceram. Int.* 43 (1) (2017) 1415–1423.
- [44] D. Yin, K. Zhang, L. Peng, Z. He, Y. Liu, H. Zhang, X. Lu, Solid-state reaction synthesis and chemical stability studies in Nd-doped zirconolite-rich ceramics, *J. Rare Earths* 36 (5) (2018) 492–498.
- [45] M. James, M.L. Carter, Z. Zhang, Y. Zhang, K.S. Wallwork, M. Avdeev, E.R. Vance, Crystal chemistry and structures of (Ca,U) titanate pyrochlores, *J. Am. Ceram. Soc.* 93 (10) (2010) 3464–3473.
- [46] W.J. Weber, J.W. Wald, H. Matzke, Effects of self-radiation damage in Cm-doped $Gd_2Ti_2O_7$ and $CaZrTi_2O_7$, *J. Nucl. Mater.* 138 (2–3) (1986) 196–209.
- [47] E.R. Vance, Synroc: a suitable waste form for actinides, *MRS Bull.* 19 (12) (1994) 28–32.
- [48] K. Zhang, S. He, D. Yin, L. Peng, J. Wu, Self-propagating synthesis and aqueous durability of Nd-bearing zirconolite-rich composites using $Ca(NO_3)_2$ as the oxidant, *J. Nucl. Mater.* 478 (2016) 315–321.
- [49] T.S. Livshits, A.A. Lizin, S.V. Tomilin, Chemical and radiation stability of ^{244}Cm -doped aluminate perovskite, *Geol. Ore Deposits* 56 (6) (2014) 440–450.
- [50] R. Grote, T. Hong, L. Shuller-Nickles, J. Amoroso, M. Tang, K.S. Brinkman, Radiation tolerant ceramics for nuclear waste immobilization: structure and stability of cesium containing hollandite of the form $(Ba,Cs)_{1.33}(Zn,Ti)_8O_{16}$ and $(Ba,Cs)_{1.33}(Ga,Ti)_8O_{16}$, *J. Nucl. Mater.* 518 (2019) 166–176.
- [51] F. Bart, H. Rabiller, G. Leturcq, D. Rigaud, Leaching behavior of hollandite ceramics for cesium immobilization, *Atalante* 1 (2004) 1–4.
- [52] M.L. Carter, Effects of sub-surface damage induced by mechanical polishing on leach testing of cesium-bearing hollandite, *Environ. Issues Waste Manag. Technol. Ceram. Nuclear Ind.* VIII (2003) 321–328.

- [53] E.R. Vance, G.R. Lumpkin, M.L. Carter, D.J. Cassidy, C.J. Ball, R.A. Day, B.D. Begg, Incorporation of Uranium in zirconolite ($\text{CaZrTi}_2\text{O}_7$), *J. Am. Ceram. Soc.* 85 (7) (2004) 1853–1859.
- [54] A. Abdelouas, S. Utsunomiya, T. Suzuki, B. Grambow, T. Advocat, F. Bart, R.C. Ewing, Effects of ionizing radiation on the hollandite structure-type: $\text{Ba}_{0.85}\text{Cs}_{0.26}\text{Al}_{1.35}\text{Fe}_{0.77}\text{Ti}_{5.90}\text{O}_{16}$, *Am. Mineral.* 93 (1) (2008) 241–247.
- [55] C.S. Dandeneau, T. Hong, K.S. Brinkman, E.R. Vance, J.W. Amoroso, Comparison of structure, morphology, and leach characteristics of multi-phase ceramics produced via melt processing and hot isostatic pressing, *J. Nucl. Mater.* 502 (2018) 113–122.
- [56] V. Luca, D. Cassidy, E. Drabarek, K. Murray, B. Moubaraki, Cesium extraction from $\text{Cs}_{0.8}\text{Ba}_{0.4}\text{Ti}_8\text{O}_{16}$ hollandite nuclear waste form ceramics in nitric acid solutions, *J. Mater. Res.* 20 (06) (2005) 1436–1446.
- [57] K.D. Reeve, *The Development and Testing of Synroc C as A High Level Nuclear Waste Form*, 1982.
- [58] K.L. Smith, G.R. Lumpkin, M.G. Blackford, R.A. Day, K.P. Hart, The durability of synroc, *J. Nucl. Mater.* 190 (C) (1992) 287–294.
- [59] R. Grote, M. Zhao, L. Shuller-Nickles, J. Amoroso, W. Gong, K. Lilova, A. Navrotsky, M. Tang, et al., Compositional control of tunnel features in hollandite-based ceramics: structure and stability of $(\text{Ba,Cs})_{1.33}(\text{Zn,Ti})_8\text{O}_{16}$, *J. Mater. Sci.* 54 (2) (2019) 1112–1125.
- [60] H. Matzke, Radiation damage-enhanced dissolution of UO_2 in water, *J. Nucl. Mater.* 190 (2) (1992) 101–106.
- [61] H. Matzke, J. Spino, Formation of the rim structure in high burnup fuel, *J. Nucl. Mater.* 248 (1997) 170–179.
- [62] V. Aubin-Chevaldonnet, D. Gourier, D. Caurant, S. Esnouf, T. Charpentier, J.M. Costantini, Paramagnetic defects induced by electron irradiation in barium hollandite ceramics for caesium storage, *J. Phys. Condens. Matter* 18 (16) (2006) 4007–4027.
- [63] J.L. Woolfrey, K.D. Reeve, D.J. Cassidy, Accelerated irradiation testing of SYNROC and its constituent minerals using fast neutrons, *J. Nucl. Mater.* 108–109 (C) (1982) 739–747.
- [64] K.A. Gowda, *Heavy Ion Bombardment of Zircon, Monazite and Other Crystal Structures*, 1982. Dissertations (1962 - 2010) Access via Proquest Digital Dissertations. AAI8228834. <https://epublications.marquette.edu/dissertations/AAI8228834>.
- [65] W.J. Weber, Effects of alpha irradiation barium hollandite and nickel iron spinel, *MRS Proc.* 44 (1984) 1–50.
- [66] K.D. Reeve, J.L. Woolfrey, Accelerated irradiation testing of synroc using fast neutrons I. First results on barium hollandite, perovskite and undoped synroc B, *J. Am. Dent. Assoc.* 86 (1980) 10–14.
- [67] R.C. Ewing, L.M. Wang, Amorphization of zirconolite: alpha-decay event damage versus krypton ion irradiation, *Nucl. Instrum. Methods Phys. Res. B* 65 (1992) 319–323.
- [68] D.R. Olander, *Fundamental Aspects of Nuclear Reactor Fuel Elements*, 1976.
- [69] W.J. Weber, R.C. Ewing, C.R.A. Catlow, T.D. de la Rubia, L.W. Hobbs, C. Kinoshita, H. Matzke, A.T. Motta, et al., Radiation effects in crystalline ceramics for the immobilization of high-level nuclear waste and plutonium, *J. Mater. Res.* 13 (06) (1998) 1434–1484.
- [70] R.C. Ewing, W.J. Weber, F.W. Clinard, Radiation effects in nuclear waste forms for high-level radioactive waste, *Prog. Nucl. Energy* 29 (2) (1995) 63–127.
- [71] S.J. Zinkle, C. Kinoshita, Defect production in ceramics, *J. Nucl. Mater.* 251 (97) (1997) 200–217.

- [72] R. Williford, R. Devanathan, W. Weber, Computer simulation of displacement energies for several ceramic materials, *Nucl. Instrum. Methods Phys. Res. Sect. B Beam Interact. Mater. Atoms* 141 (1–4) (1998) 94–98.
- [73] M. Tang, P. Tumurugoti, B. Clark, S.K. Sundaram, J. Amoroso, J. Marra, C. Sun, P. Lu, et al., Heavy ion irradiations on synthetic hollandite-type materials: Ba_{1.0}Cs_{0.3}A_{2.3}Ti_{5.7}O₁₆ (A=Cr, Fe, Al), *J. Solid State Chem.* 239 (2016) 58–63.
- [74] T. Murakami, B.C. Chakoumakos, R.C. Ewing, G.R. Lumpkin, W.J. Weber, Alpha-decay event damage in zircon, *Am. Mineral.* 76 (1991) 1510–1532.
- [75] W.J. Weber, R.C. Ewing, C.A. Angell, G.W. Arnold, A.N. Cormack, J.M. Delaye, D.L. Griscom, L.W. Hobbs, et al., Radiation effects in glasses used for immobilization of high-level waste and plutonium disposition, *J. Mater. Res.* 12 (08) (1997) 1948–1978.
- [76] F. Lu, Z. Dong, J. Zhang, T. White, R.C. Ewing, J. Lian, “Tailoring the radiation tolerance of vanadate–phosphate fluorapatites by chemical composition control, *RSC Adv.* 3 (35) (2013) 15178.
- [77] V. Aubin-Chevaldonnet, D. Gourier, D. Caurant, J.-M. Costantini, Transformation and clustering of defects induced by electron irradiation in barium hollandite ceramics for radioactive cesium storage: electron paramagnetic resonance study, *J. Appl. Phys.* 111 (8) (2012) 083504.
- [78] V. Aubin-Chevaldonnet, J.C. Badot, D. Caurant, The permittivity and the conductivity of Ba-hollandite Ba_{1.16}M_{2.32}Ti_{5.68}O₁₆ (M = Al, Ga) observed by dielectric spectroscopy, *Solid State Ionics* 178 (21–22) (2007) 1274–1281.
- [79] S. Sato, Radiation effect of simulated waste glass irradiated with ion, electron and gamma-ray, *Nucl. Instruments Methods Phys. Res. B* 1 (2–3) (1984) 534–537.
- [80] H.J. Matzke, Radiation damage effects in nuclear materials, *Nucl. Instrum. Methods Phys. Res. B* (1988) 455–470.
- [81] W.J. Weber, F.P. Roberts, *A Review of Radiation Effects in Solid Nuclear Waste Forms*, 1983.
- [82] W.J. Weber, R.C. Ewing, L.-M. Wang, The radiation-induced crystalline-to-amorphous transition in zircon, *J. Mater. Res.* 9 (03) (1994) 688–698.
- [83] S.X. Wang, L.M. Wang, R.C. Ewing, Irradiation-induced amorphization: effects of temperature, ion mass, cascade size, and dose rate, *Phys. Rev. B* 63 (2) (2000) 024105.
- [84] W.J. Weber, Models and mechanisms of irradiation-induced amorphization in ceramics, *Nucl. Instrum. Methods Phys. Res. Sect. B Beam Interact. Mater. Atoms* 166 (2000) 98–106.
- [85] S.E. Kesson, T.J. White, [Ba_xCs_y] [(Ti,Al)_{2x+y}Ti_{8-2x-y}] O₁₆ synroc-type hollandites II. Structural chemistry, *Proc. R. Soc. A Math. Phys. Eng. Sci.* 408 (1835) (1986) 295–319.
- [86] W.J. Weber, A. Navrotsky, S. Stefanovsky, E.R. Vance, E. Vernaz, Materials science of high-level immobilization, *MRS Bull.* 34 (01) (2009) 46–52.
- [87] M. Tang, J.A. Valdez, Y. Wang, J. Zhang, B.P. Uberuaga, K.E. Sickafus, Ion irradiation-induced crystal structure changes in inverse spinel MgIn₂O₄, *Scripta Mater.* 125 (2016) 10–14.
- [88] T.D. Shen, S. Feng, M. Tang, J.A. Valdez, Y. Wang, K.E. Sickafus, Enhanced radiation tolerance in nanocrystalline MgGa₂O₄, *Appl. Phys. Lett.* 90 (26) (2007) 2005–2008.
- [89] A.R. Kilmametov, D.V. Gunderov, R.Z. Valiev, A.G. Balogh, H. Hahn, Enhanced ion irradiation resistance of bulk nanocrystalline TiNi alloy, *Scripta Mater.* 59 (10) (2008) 1027–1030.

- [90] Y. Chimi, A. Iwase, N. Ishikawa, M. Kobiyama, T. Inami, S. Okuda, Accumulation and recovery of defects in ion-irradiated nanocrystalline gold, *J. Nucl. Mater.* 297 (3) (2001) 355–357.
- [91] M. Samaras, P.M. Derlet, H. Van Swygenhoven, M. Victoria, Computer simulation of displacement cascades in nanocrystalline Ni, *Phys. Rev. Lett.* 88 (12) (2002) 125505.
- [92] M. Rose, A.G. Balogh, H. Hahn, Instability of irradiation induced defects in nanostructured materials, *Nucl. Instrum. Methods Phys. Res. Sect. B Beam Interact. Mater. Atoms* 127–128 (1997) 119–122.
- [93] J. Zhang, J. Lian, A.F. Fuentes, F. Zhang, M. Lang, F. Lu, R.C. Ewing, Enhanced radiation resistance of nanocrystalline pyrochlore $\text{Gd}_2(\text{Ti}_{0.65}\text{Zr}_{0.35})_2\text{O}_7$, *Appl. Phys. Lett.* 94 (24) (2009) 2007–2010.
- [94] K.E. Sickafus, R.W. Grimes, J.A. Valdez, A. Cleave, M. Tang, M. Ishimaru, S.M. Corish, C.R. Stanek, et al., Radiation-induced amorphization resistance and radiation tolerance in structurally related oxides, *Nat. Mater.* 6 (3) (2007) 217–223.
- [95] E.M. Foltyn, F.W. Clinard, J. Rankin, D.E. Peterson, Self-irradiation effects in ^{238}Pu -substituted zirconolite: II. Effect of damage microstructure on recovery, *J. Nucl. Mater.* 136 (1) (1985) 97–103.
- [96] G.R. Lumpkin, R.C. Ewing, E.M. Foltyn, Thermal recrystallization of alpha-recoil damaged minerals of the pyrochlore structure type, *J. Nucl. Mater.* 139 (2) (1986) 113–120.
- [97] F.W. Clinard, D.S. Tucker, G.F. Hurley, C.D. Kise, Scientific basis for nuclear waste management VIII, *Mater. Res. Soc.* (1986) 663.
- [98] V. Aubin, K. Caurant, D. Gourier, N. Baffier, Radiation effects on hollandite ceramics developed for radioactive cesium immobilization, *Mater. Res. Soc. Proc.* 792 (2004) 61–67.
- [99] D.V. Stevanovic, D.A. Thompson, E.R. Vance, Rutherford backscattering investigation of radiation damage effects on the leaching of sphene and sphene-based glass-ceramics, *J. Nucl. Mater.* 161 (2) (1989) 169–174.
- [100] K. Kuramoto, H. Mitamura, T. Banba, S. Muraoka, “Development of ceramic waste forms for actinide-rich waste— radiation stability of perovskite and phase and chemical stabilities of ZR-and AL-based ceramics, *Prog. Nucl. Energy* 32 (3–4) (1998) 509–516.
- [101] F. Rabbi, K.S. Brinkman, K.L. Reifsnider, Heterogeneous materials design for sustainable nuclear waste storage using life prediction by conformal finite element analysis, in: R.E. Kirchain, B. Blanpain, C. Meskers, E. Olivetti, D. Apelian, N. Neelameggham, J. Howarter, A. Kvithyld, et al. (Eds.), *Rewas 2016 Toward Mater. Resour. Sustain.*, 2016.
- [102] K.S. Brinkman, R.K. Bordia, K.L. Reifsnider, W.K.S. Chiu, J. Amoroso, *A New Paradigm for Understanding Multiphase Ceramic Waste Form Performance*, 2014.